

# An improved 3D MoF method based on analytical partial derivatives



Xiang Chen, Xiong Zhang\*

School of Aerospace Engineering, Tsinghua University, Beijing 100084, China

## ARTICLE INFO

### Article history:

Received 24 September 2015

Received in revised form 7 August 2016

Accepted 30 August 2016

Available online 5 September 2016

### Keywords:

Surface reconstruction

Moment of fluid

Multi-material flow

## ABSTRACT

MoF (Moment of Fluid) method is one of the most accurate approaches among various surface reconstruction algorithms. As other second order methods, MoF method needs to solve an implicit optimization problem to obtain the optimal approximate surface. Therefore, the partial derivatives of the objective function have to be involved during the iteration for efficiency and accuracy. However, to the best of our knowledge, the derivatives are currently estimated numerically by finite difference approximation because it is very difficult to obtain the analytical derivatives of the object function for an implicit optimization problem. Employing numerical derivatives in an iteration not only increase the computational cost, but also deteriorate the convergence rate and robustness of the iteration due to their numerical error. In this paper, the analytical first order partial derivatives of the objective function are deduced for 3D problems. The analytical derivatives can be calculated accurately, so they are incorporated into the MoF method to improve its accuracy, efficiency and robustness. Numerical studies show that by using the analytical derivatives the iterations are converged in all mixed cells with the efficiency improvement of 3 to 4 times.

© 2016 Elsevier Inc. All rights reserved.

## 1. Introduction

Numerical simulation of fluid flow with material interface is a great challenge in computational fluid dynamics. The description of grid motion can be classified into Lagrange frame and Eulerian frame. In Lagrangian frame, the computational grid is embedded with material so the material interface is always the grid boundary which can be traced innately. However, in Lagrangian frame, the computation will fall into stagnation with increasing grid distortion because fluid material will always experience a large deformation with respect to time. On the contrary, the computational grid is fixed in Euler frame which overcomes the grid distortion but loses the surface information because it advects across the grid during the simulation. In order to track the material interfaces, extra efforts are required.

Level-set method and VoF (Volume of Fluid) method are two major approaches for surface reconstruction. Level-set method [1–3] constructs the surface by an implicit distance function whose zero contour is the location of the surface. This method avoids complicate geometric analysis but on the other hand, the level-set equation must be solved in high order of accuracy to avoid serious dissipation which triggers a high level of volume loss especially in unstructured grid [1]. VoF method [4–10] explicitly constructs such an approximate linear surface in every mix cell that the total volume of every

\* Corresponding author.

E-mail address: xzhang@tsinghua.edu.cn (X. Zhang).

material is conserved. VoF method is independent of grid type so it can be performed in both structured and unstructured grid.

The approximate surface  $\mathbf{n} \cdot \mathbf{x} + d = 0$  in a cell is constructed in VoF method in two steps. The first step determines the normal  $\mathbf{n}$  of the linear surface and the second step calculates the constant  $d$  which satisfies the local volume enforcement, namely, the volume fraction of the polyhedron below the approximate material interface must exactly equal to the given volume fraction in the cell. The second step in different kinds of VoF method is almost the same because the constant  $d$  can be determined uniquely as long as  $\mathbf{n}$  and volume fraction are given. It can be calculated by an iterative or analytical approach. In 3D problems, the analytical solver is only suitable for simple polyhedron such as tetrahedron [7] or regular hexahedron [11] but for complicate grid such as generalized hexahedron, which is widely used in ALE method [12,13], the iterative method is a better choice [14].

The most important part in a VoF method is the first step because the estimation of  $\mathbf{n}$  plays a significant role in the accuracy of surface reconstruction. Youngs' method [8–10] estimates the normal  $\mathbf{n}$  by the gradient of volume fraction which comes from the volume fraction of adjacent cells. This estimation can be calculated directly without iterative process but it is only first order accurate which even can not reconstruct linear surface precisely. For the sake of second order accuracy, additional requirement was proposed besides the local volume enforcement. LVIRA (Least square Volume Interface Reconstruction Algorithm) [5] estimates the normal by finding a linear interface, which will be extended outside the mix cell, to minimize the discrepancy of volume fraction in adjacent cells. ELVIRA (Efficient least squares VOF interface reconstruction algorithm) [5] presents an alternative minimization approach by determining the normal from six candidates which is also second order accurate and does not require iterative process. Swartz method [15,16] calculates the normal by finding a common linear interface for a pair of neighbor mix cells which rigorously satisfies the given volume fraction. These methods are second order accurate but an implicit optimization is usually required to be solved in order to determine the appropriate normal except for the ELVIRA method which can only be performed on structured grid. Therefore the iterative process is inevitable for unstructured grid. All these methods need the volume fraction from adjacent cells and extra treatments have to be implemented for boundary cells which lead to increasing difficulty in programming and parallelization.

MoF (Moment of Fluid) method [17–19] is a new approach to estimate  $\mathbf{n}$  in a cell which takes use of both the volume fraction and the material centroid of the cell. It calculates the normal  $\mathbf{n}$  by finding a linear surface which minimize the discrepancy between the given reference material centroid and the approximate material centroid. MoF method is also second order accurate which can reconstruct linear interface exactly. Moreover, this method is more accurate than previous second order VoF methods in fluid simulation [20]. Despite the higher accuracy, another attractive superiority of MoF method is that it does not need any information from neighbor cells. This feature allows MoF method to be implemented as a cell-by-cell black-box routine, which is a great predominance over other VoF methods. Alike to LVIRA [5] and Swartz method [15,16], an implicit nonlinear optimization problem is also needed to be solved and an iterative process is unavoidable.

Whenever the normal  $\mathbf{n}$  is changed during the iterative process, the constant  $d$  has to be recalculated to update the objective function which is a heavy expenditure especially for 3D problem. Therefore, in order to reduce the number of the objective function calculations and solve the optimization problem efficiently and accurately, its derivatives must be used in the iterative process. In 2D problem, Dyadechko and Shashkov [21] presented the first-order derivative of the objective function and Lemoine et al. [22] deduced the analytic solution of the normal  $\mathbf{n}$  on a rectangular grid without solving a nonlinear optimization problem. However, to the best of our knowledge, the derivatives of the objective function in 3D MoF method are currently estimated by numerical difference due to the nonlinearity and implicitness of the objective function. Numerical difference needs extra calculations of the objective function and the error in the differential approximation may also deteriorate the convergence rate and robustness of the iteration.

In this paper, the analytical first order partial derivatives of the objective function in MoF method are deduced for 3D problems. Little extra effort is needed in calculating the analytical derivatives and they can be calculated accurately. Moreover, the analytical derivatives not only accelerate the convergence of iteration but also improve its robustness. Numerical experiments show that iteration using the analytical derivatives is about 3 to 4 times faster than that using the numerical derivatives.

The rest of this paper is organized as follow. The local volume enforcement requirement is briefly reviewed in Section 2, while the normal estimation by MoF method is introduced in Section 3. A centroid rotation rule to fulfill the local volume enforcement is proposed in Section 4 and then the analytical derivatives are deduced in Section 5. Several numerical tests are presented in Section 6 to validate our analytical derivatives and demonstrate their advantages. Finally, Section 7 concludes this paper.

## 2. Local volume enforcement requirement

Local volume enforcement is a fundamental requirement in any VoF surface reconstruction algorithm. As shown in Fig. 1, if the normal  $\mathbf{n}$  of the approximate plane surface is given, there will be a series of parallel planes with different constant  $d$ , such as  $\mathbf{n} \cdot \mathbf{x} + d_1 = 0$ ,  $\mathbf{n} \cdot \mathbf{x} + d_2 = 0$  and  $\mathbf{n} \cdot \mathbf{x} + d_3 = 0$ . Each plane is intersected with the grid and a new polyhedron below the plane is generated. For instance the polyhedron  $\mathbb{P}p_1p_2p_3p_4CD$  is generated from  $\mathbf{n} \cdot \mathbf{x} + d_1 = 0$  in Fig. 1. Therefore, the volume of the new generated polyhedron  $V_{\text{below}}$  can be uniquely determined by the constant  $d$ , namely  $V_{\text{below}} = V(d)$  so its volume fraction is  $v = v(d) = V(d) / V_{\text{cell}}$ , where  $V_{\text{cell}}$  is the total volume of the mix cell. The local volume enforcement

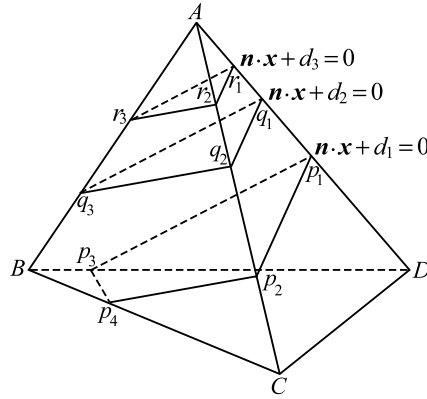


**Fig. 1.** The local volume enforcement. Different constants  $d$  determine different surfaces and the volume fraction below the approximate surface must equal to the given volume fraction  $v^{\text{ref}}$ .

requires the volume fraction of the new generated polyhedron below the approximate surface must equal to the given reference volume fraction  $v^{\text{ref}}$ , namely Eq. (1) must be solved for  $d^*$  to obtain the approximate surface  $\mathbf{n} \cdot \mathbf{x} + d^* = 0$ .

$$v(d^*) = v^{\text{ref}} \tag{1}$$

This requirement ensures the total material volume is conserved during the surface reconstruction.

The clipping and capping algorithm [14,23] is used here to calculate the volume fraction  $v(d)$ , which first calculates the intersected vertexes on the cutting plane, namely the approximate surface, and then generates a new polyhedron below the cutting plane. For example, the intersected vertexes on the cutting plane  $\mathbf{n} \cdot \mathbf{x} + d_1 = 0$  are  $p_1, p_2, p_3$  and  $p_4$ , and the new generated polyhedron below the cutting plane is  $\mathbb{P}p_1p_2p_3p_4CD$ . Finally it converts the volume integral to surface integrals on each face by Gauss's theorem. It is obvious that  $v(d)$  is rigorously monotonous with  $v(d_{\min}) = 0$  and  $v(d_{\max}) = 1$  so there will be a unique  $d^*$  that fulfills Eq. (1). On the other hand,  $v(d)$  is a nonlinear and implicit function so an iteration process is inevitable. The bisection or secant method was used for iteration in Ahn and Shashkov (2008) [14], whereas the Brent's iteration method is used in this paper.

It should be mentioned that the coordinates of the vertexes on the cutting plane obtained in this process are sufficient for constructing the analytical derivatives in Section 5.

The plane constant  $d$  can be uniquely calculated by the local volume enforcement once the normal  $\mathbf{n}$  of the approximate surface is determined, so the accuracy of the approximate surface is dependent on the normal estimation. The normal estimation by MoF method seems to be the most promising one compared with other approaches because it is more accurate [18–20] and does not need any information from neighbor cells. For material  $i$ , MoF method estimates the normal by minimizing the discrepancy between the given reference material centroid  $\mathbf{x}_{m,i}^{\text{ref}}$  and the approximate material centroid  $\mathbf{x}_{m,i}(\mathbf{n})$ , namely calculating a particular  $\mathbf{n}_i^*$  to minimize the following function:

$$f_i(\mathbf{n}) = \left\| \mathbf{x}_{m,i}(\mathbf{n}) - \mathbf{x}_{m,i}^{\text{ref}} \right\| \tag{2}$$

where  $\|\cdot\|$  represents the L2 norm squared. The material centroid is defined as

$$\mathbf{x}_{m,i} = \frac{\int_{\Pi_i} (x, y, z) dx dy dz}{\int 1 dx dy dz} \tag{3}$$

where  $\Pi_i$  is the domain occupied by the material  $i$ . In following discussions, all formulations are associated with material  $i$  so that the subscript  $i$  is omitted.

### 3. Normal estimation by MoF method

The normal  $\mathbf{n}$  can be represented by two parameters  $\theta$  and  $\varphi$  in space, i.e.  $\mathbf{n} = (\sin\theta \cos\varphi, \sin\theta \sin\varphi, \cos\theta)$ , so that Eq. (2) can be rewritten as

$$f(\theta, \varphi) = \left\| \mathbf{x}_m(\theta, \varphi) - \mathbf{x}_m^{\text{ref}} \right\| \tag{4}$$

The objective function  $f(\theta, \varphi)$  is implicit because  $\mathbf{x}_m(\theta, \varphi)$  has to be calculated from Eq. (1), so an iteration process is inevitable in solving the optimization problem. Whenever  $\theta$  or  $\varphi$  changes during the iteration, the local volume enforcement process have to be performed to update the objective function which is very expensive. Therefore, in order to reduce the number of the objective function calculations and solve the optimization problem efficiently and accurately, its derivatives

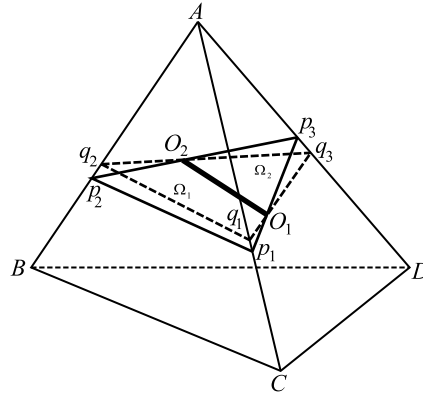


**Fig. 2.** Infinitesimal rotation of the approximate surface. The derived triangle  $\mathbb{T}q_1q_2q_3$  is generated by an infinitesimal rotation of the base surface  $\mathbb{T}p_1p_2p_3$  about an arbitrary line  $O_1O_2$ . The polyhedrons  $\mathbb{P}p_1p_2q_1q_2O_1O_2$  and  $\mathbb{P}p_3q_3O_1O_2$  are denoted by  $\Omega_1$  and  $\Omega_2$ , respectively, and the dihedral angle between the base and derived triangle will be denoted by  $\Delta\alpha$ .

should be used in the iteration. However, due to the nonlinearity and implicitness of the objective function, the derivatives are currently approximated by their numerical differences in the literature and two extra local volume enforcement equations have to be solved to calculate  $f(\theta + \Delta\theta, \varphi)$  and  $f(\theta, \varphi + \Delta\varphi)$ . Moreover, the error in these approximated derivatives may deteriorate the convergence rate and robustness of the iteration. In this paper, the analytical first order partial derivatives of the objective function are firstly deduced, which allows the derivatives and the objective function could be calculated simultaneously, and then incorporated into the MoF method to improve its accuracy, efficiency and robustness.

In order to deduce the analytical expression, just as the previous work by Dyadechko and Shashkov [21], these derivatives can be rewritten by the chain rule as

$$\frac{\partial f}{\partial \theta} = 2[\mathbf{x}_m(\theta, \varphi) - \mathbf{x}_m^{\text{ref}}] \cdot \frac{\partial \mathbf{x}_m(\theta, \varphi)}{\partial \theta} \tag{5}$$

$$\frac{\partial f}{\partial \varphi} = 2[\mathbf{x}_m(\theta, \varphi) - \mathbf{x}_m^{\text{ref}}] \cdot \frac{\partial \mathbf{x}_m(\theta, \varphi)}{\partial \varphi} \tag{6}$$

In practice, once the constant  $d^*$  of the approximate surface  $\mathbf{n} \cdot \mathbf{x} + d^* = 0$  is obtained from the local volume enforcement Eq. (1), the polyhedron below the approximate surface can be constructed, so that  $\mathbf{x}_m(\theta, \varphi)$  in Eq. (5) and Eq. (6) can be calculated accurately from Eq. (3) by converting the volume integral to surface integrals on each face. Therefore, our major objective is to deduce the analytical expression for  $\partial \mathbf{x}_c(\theta, \varphi) / \partial \theta$  and  $\partial \mathbf{x}_c(\theta, \varphi) / \partial \varphi$ .

#### 4. Centroid rotation rule

Based on the definition of a derivative,  $\partial \mathbf{x}_c(\theta, \varphi) / \partial \theta$  and  $\partial \mathbf{x}_c(\theta, \varphi) / \partial \varphi$  can be reformulated as

$$\frac{\partial \mathbf{x}_m(\theta, \varphi)}{\partial \theta} = \lim_{\Delta\theta \rightarrow 0} \frac{\mathbf{x}_m(\theta + \Delta\theta, \varphi) - \mathbf{x}_m(\theta, \varphi)}{\Delta\theta} \tag{7}$$

$$\frac{\partial \mathbf{x}_m(\theta, \varphi)}{\partial \varphi} = \lim_{\Delta\varphi \rightarrow 0} \frac{\mathbf{x}_m(\theta, \varphi + \Delta\varphi) - \mathbf{x}_m(\theta, \varphi)}{\Delta\varphi} \tag{8}$$

The  $\Delta\theta$  and  $\Delta\varphi$  in Eq. (7) and Eq. (8) represent an infinitesimal rotation of the approximate surface about two specific lines. For the sake of clarity, a tetrahedron is illustrated in Fig. 2, but the deduction given below is also valid for any complex polyhedrons. It should be mentioned that when calculating the partial derivatives, only two specific rotation axes are considered, but in general, the rotation can be about an arbitrary axis. As shown in Fig. 2, the triangles  $\mathbb{T}p_1p_2p_3$  and  $\mathbb{T}q_1q_2q_3$  are termed as the base approximate surface and derived approximate surface respectively. The derived surface  $\mathbb{T}q_1q_2q_3$  is obtained by an infinitesimal rotation of the base surface  $\mathbb{T}p_1p_2p_3$  about an arbitrary axis  $O_1O_2$  and the dihedral angle between them is denoted by  $\Delta\alpha$ , as illustrated in Fig. 3. In this section, we will prove that in order to make the derived surface fulfill the local volume enforcement, the base surface must be rotated around its centroid. This centroid rotation rule is not only valid for MoF method, but also applicable for any VoF algorithm.

##### 4.1. Approximate alternative columns

Local volume enforcement in Fig. 2 requires

$$V_{\mathbb{P}p_1p_2p_3CBD} = V_{\mathbb{P}q_1q_2q_3CDB} \tag{9}$$

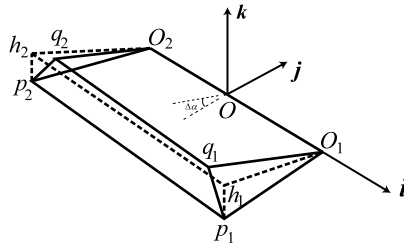


Fig. 3. The local coordinate system and the alternative column  $\mathbb{P}_{p_1p_2O_1O_2h_1h_2}$  for the polyhedron  $\Omega_1$ .

where  $V$  denotes the volume of a polyhedron. Subtracting the common portion  $\mathbb{P}_{p_1p_2O_1O_2q_3CBD}$  from both sides of Eq. (9) leads to

$$V_{\mathbb{P}_{p_1p_2q_1q_2O_1O_2}} = V_{\mathbb{P}_{p_3q_3O_1O_2}} \tag{10}$$

Denoting the polyhedron  $\mathbb{P}_{p_1p_2q_1q_2O_1O_2}$  as  $\Omega_1$  and polyhedron  $\mathbb{P}_{p_3q_3O_1O_2}$  as  $\Omega_2$ , Eq. (10) can be rewritten as

$$\int_{\Omega_1} dV = \int_{\Omega_2} dV \tag{11}$$

Thus, Eq. (7) and Eq. (8) can be reduced to

$$\frac{\partial \mathbf{x}_m(\theta, \varphi)}{\partial \theta} = \lim_{\Delta\theta \rightarrow 0} \frac{\int_{\Omega_1} \mathbf{x}dV - \int_{\Omega_2} \mathbf{x}dV}{V^{\text{ref}} \Delta\theta} \tag{12}$$

$$\frac{\partial \mathbf{x}_m(\theta, \varphi)}{\partial \varphi} = \lim_{\Delta\varphi \rightarrow 0} \frac{\int_{\Omega_1} \mathbf{x}dV - \int_{\Omega_2} \mathbf{x}dV}{V^{\text{ref}} \Delta\varphi} \tag{13}$$

The polyhedrons  $\Omega_1$  and  $\Omega_2$  are arbitrary polyhedrons, so the volume integrals on them are complicated to calculate. To simplify the volume integration on these two polyhedrons, we construct two columns  $\Omega'_1$  and  $\Omega'_2$  to approximate the polyhedrons  $\Omega_1$  and  $\Omega_2$  respectively because the volume integration on a column is much more easier to be calculated as shown in Appendix A. The constructed approximate columns must fulfill the requirement

$$\left( \int_{\Omega_1} \mathbf{x}dV - \int_{\Omega_2} \mathbf{x}dV \right) - \left( \int_{\Omega'_1} \mathbf{x}dV - \int_{\Omega'_2} \mathbf{x}dV \right) = O(\Delta\alpha^2) \tag{14}$$

We will prove that as long as Eq. (14) is satisfied, the RHS of Eq. (12) and Eq. (13) integrating on the original regions  $\Omega_1$  and  $\Omega_2$  are equivalent to those integrating on the approximate regions  $\Omega'_1$  and  $\Omega'_2$ .

The infinitesimal increments in  $\theta$  and  $\varphi$ , namely  $\Delta\theta$  and  $\Delta\varphi$ , will lead to infinitesimal dihedral angles  $\Delta\alpha_\theta$  and  $\Delta\alpha_\varphi$  but they may not be equal. Nevertheless, the conclusion in Section 5.1 shows that they are in the same order. Therefore, if Eq. (14) is fulfilled, the RHS of Eq. (12) can be rewritten as

$$\begin{aligned} \frac{\int_{\Omega_1} \mathbf{x}dV - \int_{\Omega_2} \mathbf{x}dV}{V^{\text{ref}} \Delta\theta} &= \frac{\int_{\Omega'_1} \mathbf{x}dV - \int_{\Omega'_2} \mathbf{x}dV + O(\Delta\alpha_\theta^2)}{V^{\text{ref}} \Delta\theta} \\ &= \frac{\int_{\Omega'_1} \mathbf{x}dV - \int_{\Omega'_2} \mathbf{x}dV}{V^{\text{ref}} \Delta\theta} + O(\Delta\theta) \end{aligned} \tag{15}$$

where the second line results from the fact that  $\Delta\alpha_\theta$  is in the same order as  $\Delta\theta$ . Substituting Eq. (15) into Eq. (12) gives

$$\frac{\partial \mathbf{x}_m(\theta, \varphi)}{\partial \theta} = \lim_{\Delta\theta \rightarrow 0} \frac{\int_{\Omega'_1} \mathbf{x}dV - \int_{\Omega'_2} \mathbf{x}dV}{V^{\text{ref}} \Delta\theta} \tag{16}$$

Similarly,

$$\frac{\partial \mathbf{x}_m(\theta, \varphi)}{\partial \varphi} = \lim_{\Delta\varphi \rightarrow 0} \frac{\int_{\Omega'_1} \mathbf{x}dV - \int_{\Omega'_2} \mathbf{x}dV}{V^{\text{ref}} \Delta\varphi} \tag{17}$$

In summary, the first order partial derivatives calculated on the original polyhedrons are identical to those calculated on the alternative columns.

In order to simplify the derivation, we employ a local coordinate system for the polyhedron  $\mathbb{P}_{p_1p_2q_1q_2O_1O_2}$ , as shown in Fig. 3. The origin of the local coordinate system lies on the rotation line  $O_1O_2$ , axis  $i$  is along  $\overrightarrow{O_2O_1}$ , axis  $k$  is along the

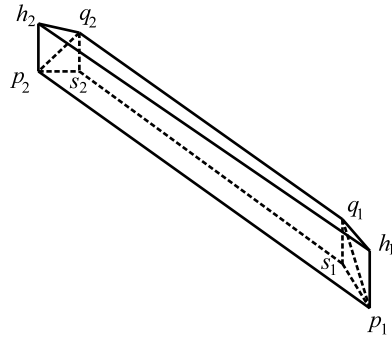


**Fig. 4.** The error polyhedron  $\mathbb{P}p_1p_2h_1h_2q_1q_2$ , and the auxiliary polyhedron  $\mathbb{P}q_1q_2h_1h_2s_1s_2$ . Eq. (18) guarantees the integral on the error polyhedron is  $O(\Delta\alpha^2)$ .

normal of the base surface  $p_1p_2O_1O_2$  and axis  $\mathbf{j} = \mathbf{k} \times \mathbf{i}$ . The integrals will be calculated in this local coordinate system. To construct an alternative column for the polyhedron  $\Omega_1$ , two auxiliary lines are created passing through the vertices  $p_1$  and  $p_2$  and perpendicular to the base surface  $p_1p_2O_1O_2$ . They will intersect with the derived surface  $q_1q_2O_1O_2$  at  $h_1$  and  $h_2$  and we will show that the alternative column  $\mathbb{P}p_1p_2O_1O_2h_1h_2$  fulfills Eq. (14).

As shown in Fig. 3, the LHS of Eq. (14) involves the integrals on three error polyhedrons, namely,  $\mathbb{P}p_1p_2h_1h_2q_1q_2$ ,  $\mathbb{P}p_1h_1q_1O_1$  and  $\mathbb{P}p_2h_2q_2O_2$ . As  $h_1, h_2, q_1, q_2, O_1$  and  $O_2$  are all located on the derived surface, the integral on  $\mathbb{P}h_1h_2q_1q_2O_1O_2$  equals to zero. Generally speaking, the number of error polyhedrons is always finite. Therefore, Eq. (14) is fulfilled as long as the integral error on every error polyhedron is  $O(\Delta\alpha^2)$ . Take the polyhedron  $\mathbb{P}p_1p_2h_1h_2q_1q_2$  in Fig. 3 as an example, which has been amplified in Fig. 4 for the sake of clarity. Create two points  $s_1$  and  $s_2$  such that  $q_1s_1$  and  $q_2s_2$  are perpendicular to the base surface, so the polyhedron  $\mathbb{P}p_1p_2s_1s_2q_1q_2h_1h_2$  is a column. The following inequality ensures the integral error is  $O(\Delta\alpha^2)$  where  $f = 1, g = 1$  for volume calculation,  $f = x, y, z, g = x, y, 0.5z$  for centroid calculation.

$$\begin{aligned} \left| \int_{p_1p_2q_1q_2h_1h_2} f dV \right| &\leq \left| \int_{p_1p_2q_1q_2h_1h_2s_1s_2} f dV \right| = \left| n_z \oint_{q_1q_2h_1h_2} zgdS \right| \\ &\leq |n_z z_{\max} g_{\max} S_{q_1q_2h_1h_2}| = \left| n_z z_{\max} g_{\max} \frac{S_{p_1p_2s_1s_2}}{|n_z|} \right| \\ &= |z_{\max} g_{\max} S_{p_1p_2s_1s_2}| = O(\Delta\alpha^2) \end{aligned} \tag{18}$$

where  $n_z$  is the third component of the unit normal of the derived surface in the local coordinate system  $Oxyz$  and  $S_{p_1p_2s_1s_2}$  is the area of the bottom-surface of the column.

The first inequality in Eq. (18) is due to  $\mathbb{P}p_1p_2q_1q_2h_1h_2 \subseteq \mathbb{P}p_1p_2q_1q_2h_1h_2s_1s_2$  and the subsequent equality is a consequence of Eq. (A.4) to Eq. (A.7) in Appendix A. Finally, it can be proven that  $z_{\max} = O(\Delta\alpha)$  and  $S_{p_1p_2h_1h_2} = O(\Delta\alpha)$  and  $g_{\max}$  is finite on face  $q_1q_2h_1h_2$  thus the last equality is fulfilled.

In summary, the volume integral domains  $\Omega_1$  and  $\Omega_2$  in Eq. (12) and Eq. (13) can be replaced by their approximate alternative columns for calculating the first order partial derivatives. The approximate alternative columns make the integrals much easier to be calculated so they will be used in next sections.

#### 4.2. Centroid rotation rule

According to the volume integral approximation, the left side of Eq. (11) can be rewritten as

$$\int_{\Omega_1} dV \approx \int_{\Omega'_1} dV = \int_{\mathbb{P}p_1p_2O_1O_2h_1h_2} dV \tag{19}$$

The polyhedron  $\mathbb{P}p_1p_2O_1O_2h_1h_2$  is a column, so according to Eq. (A.4), the above volume integral can be further simplified as

$$\int_{\Omega'_1} dV = n_z \oint_{O_1O_2h_1h_2} z dS \tag{20}$$

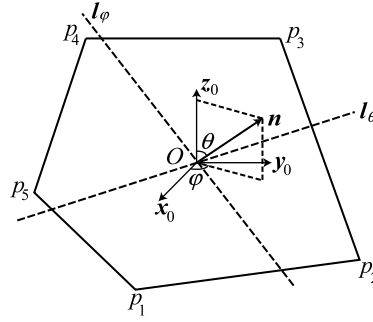


Fig. 5. Rotation direction for partial derivatives.

In order to find the right hand side of Eq. (20), the equation of the derived surface,  $O_1O_2h_1h_2$ , in the local coordinate system  $Oxyz$  in Fig. 3 is  $y \sin(\Delta\alpha) + z \cos(\Delta\alpha) = 0$ , namely  $z = -y \sin(\Delta\alpha) / \cos(\Delta\alpha)$ . Substituting this relation into Eq. (A.4) leads to

$$\int_{\Omega_1'} dV = \text{sign}(n_z) \frac{\sin(\Delta\alpha)}{\cos(\Delta\alpha)} \oint_{p_1p_2O_1O_2} y dx dy = -\frac{\sin(\Delta\alpha)}{\cos(\Delta\alpha)} \oint_{p_1p_2O_1O_2} y dx dy \tag{21}$$

Similarly, the right side of Eq. (11) can be approximated as

$$\int_{\Omega_2} dV \approx \int_{\Omega_2'} dV = \text{sign}(n_z) \frac{\sin(\Delta\alpha)}{\cos(\Delta\alpha)} \oint_{p_3O_1O_2} y dx dy = \frac{\sin(\Delta\alpha)}{\cos(\Delta\alpha)} \oint_{p_3O_1O_2} y dx dy \tag{22}$$

The sign of Eq. (21) and Eq. (22) is opposite because the outward normal  $n_z$  of the derived surface is opposite. Substituting Eq. (21) and Eq. (22) into Eq. (11), the local volume enforcement requirement gives

$$\oint_{p_3O_1O_2} y dx dy + \oint_{p_1p_2O_1O_2} y dx dy = \oint_{p_1p_2p_3} y dx dy = 0 \tag{23}$$

Eq. (23) indicates that the centroid of the base surface  $p_1p_2p_3$  must lie on the rotation axis  $O_1O_2$ . Moreover, because the direction of rotation is arbitrary, the base surface must rotate around its centroid to fulfill the local volume enforcement.

It should be mentioned again that the centroid rotation rule is not only valid for MoF method, but also a general requirement for any VoF methods whenever the normal of approximate surface is changed.

### 5. First order analytical partial derivatives

#### 5.1. The rotation axes for partial derivatives

The centroid rotation rule is valid for any rotation axis, however, for calculating the partial derivatives, the rotation is performed about two specific axes. As shown in Fig. 5,  $p_1p_2p_3p_4p_5$  is a base surface,  $O$  is its centroid,  $\mathbf{x}_0, \mathbf{y}_0, \mathbf{z}_0$  are the global coordinate system axes,  $\mathbf{n}$  is the normal of the base surface and  $\mathbf{l}_\theta, \mathbf{l}_\varphi$  are the unit vectors of the rotation axis for  $\theta$  and  $\varphi$ . It is obvious that  $\mathbf{l}_\theta$  must be perpendicular to  $\mathbf{n}(\theta, \varphi)$  and  $\mathbf{n}(\theta + \Delta\theta, \varphi)$  and  $\mathbf{l}_\varphi$  must be perpendicular to  $\mathbf{n}(\theta, \varphi)$  and  $\mathbf{n}(\theta, \varphi + \Delta\varphi)$ , namely

$$\mathbf{l}_\theta = \lim_{\Delta\theta \rightarrow 0} \frac{\mathbf{n}(\theta + \Delta\theta, \varphi) \times \mathbf{n}(\theta, \varphi)}{\|\mathbf{n}(\theta + \Delta\theta, \varphi) \times \mathbf{n}(\theta, \varphi)\|} = (\sin \varphi, -\cos \varphi, 0) \tag{24}$$

The relation between the infinitesimal dihedral angle  $\Delta\alpha_\theta$  and the infinitesimal increment of  $\theta$  can be obtained by the following equation:

$$\lim_{\Delta\theta \rightarrow 0} \frac{\Delta\alpha_\theta}{\Delta\theta} = \lim_{\Delta\theta \rightarrow 0} \frac{\sin(\Delta\alpha_\theta)}{\sin(\Delta\theta)} = \lim_{\Delta\theta \rightarrow 0} \frac{\|\mathbf{n}(\theta + \Delta\theta, \varphi) \times \mathbf{n}(\theta, \varphi)\|}{\sin(\Delta\theta)} = 1 \tag{25}$$

where the subscript  $\theta$  means the dihedral angle  $\Delta\alpha$  is caused by the increment of  $\theta$  with  $\varphi$  fixed. Namely,  $\Delta\alpha_\theta$  and  $\Delta\theta$  are in the same order and  $\Delta\alpha_\theta$  is equivalent with  $\Delta\theta$ . Similarly we have

$$\mathbf{l}_\varphi = \lim_{\Delta\varphi \rightarrow 0} \frac{\mathbf{n}(\theta, \varphi + \Delta\varphi) \times \mathbf{n}(\theta, \varphi)}{\|\mathbf{n}(\theta, \varphi + \Delta\varphi) \times \mathbf{n}(\theta, \varphi)\|} = (\cos\theta \cos\varphi, \cos\theta \sin\varphi, -\sin\theta) \tag{26}$$

$$\lim_{\Delta\varphi \rightarrow 0} \frac{\Delta\alpha_\varphi}{\Delta\varphi} = \lim_{\Delta\varphi \rightarrow 0} \frac{\sin(\Delta\alpha_\varphi)}{\sin(\Delta\varphi)} = \lim_{\Delta\varphi \rightarrow 0} \frac{\|\mathbf{n}(\theta, \varphi + \Delta\varphi) \times \mathbf{n}(\theta, \varphi)\|}{\sin(\Delta\varphi)} = \sin\theta \tag{27}$$

which indicates that  $\Delta\alpha_\varphi$  and  $\Delta\varphi$  are in the same order and  $\Delta\alpha_\varphi$  is equivalent with  $\sin\theta\Delta\varphi$ .

Once  $\mathbf{l}_\theta$  or  $\mathbf{l}_\varphi$  is obtained, the local coordinate system in Fig. 3 can be determined:  $O$  is the centroid of the base surface,  $\mathbf{k} = \mathbf{n}$ ,  $\mathbf{i} = \mathbf{l}_\theta$  or  $\mathbf{i} = \mathbf{l}_\varphi$  and  $\mathbf{j} = \mathbf{k} \times \mathbf{i}$ . Therefore, the unit vectors of the two local coordinate systems are  $\mathbf{i}_\theta = (\sin\varphi, -\cos\varphi, 0)$ ,  $\mathbf{j}_\theta = (\cos\theta \cos\varphi, \cos\theta \sin\varphi, -\sin\theta)$  and  $\mathbf{i}_\varphi = (\cos\theta \cos\varphi, \cos\theta \sin\varphi, -\sin\theta)$ ,  $\mathbf{j}_\varphi = (-\sin\varphi, \cos\varphi, 0)$ , respectively. Comparing the parameters we have  $\mathbf{i}_\theta = -\mathbf{j}_\varphi$  and  $\mathbf{j}_\theta = \mathbf{i}_\varphi$ , so the coordinates in these two local system fulfill

$$x_\varphi = y_\theta \tag{28}$$

$$y_\varphi = -x_\theta \tag{29}$$

### 5.2. The analytical derivatives

The partial derivatives are the dot product of two vectors according to Eq. (5) and Eq. (6), which are independent of the choice of coordinate system, so they will be calculated in the local coordinate system defined in Section 5.1. As illustrated in Section 4, the equation of the derived surface in the new coordinate system is  $z = -y \sin(\Delta\alpha) / \cos(\Delta\alpha)$ . Substitute this relation into Eqs. (A.5) to (A.7), the integrals in Eq. (12) are calculated as

$$\int_{\Omega'_1} x dV = -\frac{\sin(\Delta\alpha)}{\cos(\Delta\alpha)} \oint_{p_1 p_2 O_1 O_2} xy dx dy \tag{30}$$

$$\int_{\Omega'_1} y dV = -\frac{\sin(\Delta\alpha)}{\cos(\Delta\alpha)} \oint_{p_1 p_2 O_1 O_2} y^2 dx dy \tag{31}$$

$$\int_{\Omega'_1} z dV = -\frac{1}{2} \frac{\sin^2(\Delta\alpha)}{\cos^2(\Delta\alpha)} \oint_{p_1 p_2 O_1 O_2} y^2 dx dy \tag{32}$$

and

$$\int_{\Omega'_2} x dV = \frac{\sin(\Delta\alpha)}{\cos(\Delta\alpha)} \oint_{p_3 O_1 O_2} xy dx dy \tag{33}$$

$$\int_{\Omega'_2} y dV = \frac{\sin(\Delta\alpha)}{\cos(\Delta\alpha)} \oint_{p_3 O_1 O_2} y^2 dx dy \tag{34}$$

$$\int_{\Omega'_2} z dV = \frac{1}{2} \frac{\sin^2(\Delta\alpha)}{\cos^2(\Delta\alpha)} \oint_{p_3 O_1 O_2} y^2 dx dy \tag{35}$$

Therefore, Eq. (12) can be written as

$$\frac{\partial \mathbf{x}_m(\theta, \varphi)}{\partial \theta} = \lim_{\Delta\theta \rightarrow 0} \frac{-\sin(\Delta\alpha_\theta)}{V^{\text{ref}} \Delta\theta \cos(\Delta\alpha_\theta)} \left( I_{xy}, I_{yy}, \frac{1}{2} \frac{\sin(\Delta\alpha_\theta)}{\cos(\Delta\alpha_\theta)} I_{yy} \right) \tag{36}$$

$$\frac{\partial \mathbf{x}_m(\theta, \varphi)}{\partial \varphi} = \lim_{\Delta\varphi \rightarrow 0} \frac{-\sin(\Delta\alpha_\varphi)}{V^{\text{ref}} \Delta\varphi \cos(\Delta\alpha_\varphi)} \left( I_{xy}, I_{yy}, \frac{1}{2} \frac{\sin(\Delta\alpha_\varphi)}{\cos(\Delta\alpha_\varphi)} I_{yy} \right) \tag{37}$$

where

$$I_{xy} = \oint_{p_1 p_2 p_3} xy dx dy, \quad I_{xx} = \oint_{p_1 p_2 p_3} x^2 dx dy, \quad I_{yy} = \oint_{p_1 p_2 p_3} y^2 dx dy \tag{38}$$

Substitute Eq. (25) and Eq. (27) into Eq. (36) and Eq. (37) and then make limit, the analytical partial derivatives are obtained as

$$\frac{\partial \mathbf{x}_m(\theta, \varphi)}{\partial \theta} = -\frac{1}{V^{\text{ref}}} (I_{x_\theta y_\theta}, I_{y_\theta y_\theta}, 0) \tag{39}$$

$$\frac{\partial \mathbf{x}_m(\theta, \varphi)}{\partial \varphi} = -\frac{1}{V^{\text{ref}}} \sin\theta (I_{x_\varphi y_\varphi}, I_{y_\varphi y_\varphi}, 0) \tag{40}$$

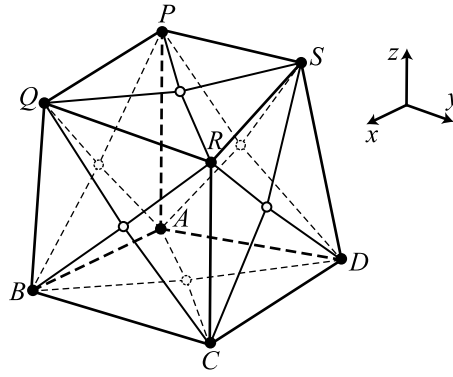


Fig. 6. Single cell test. The solid dots represent the vertices, whereas the hollow dots represent the face centers.

It should be mentioned that the coordinate systems used in Eq. (39) and Eq. (40) are different, but according to Eq. (28) and Eq. (29), the partial derivative with respect to  $\varphi$  can be rewritten as

$$\frac{\partial \mathbf{x}_m(\theta, \varphi)}{\partial \varphi} = -\frac{1}{V^{\text{ref}}} \sin \theta (-I_{x_\theta y_\theta}, I_{x_\theta x_\theta}, 0) \quad (41)$$

The integrand in Eq. (39) and Eq. (41) are quadratic functions, so in order to calculate the integral exactly on the polygon, one of the simplest method is to decompose this polygon into triangles and use 3-point Gauss quadrature rule to obtain the integral in each triangle. Subsequently, substitute Eq. (39) and Eq. (41) into Eq. (5) and Eq. (6), the partial derivatives of the function  $f(\theta, \varphi)$  can be calculated. The expression of partial derivatives in Eq. (39) and (41) are analytical and the integral  $I_{x_\theta y_\theta}$ ,  $I_{y_\theta y_\theta}$ ,  $I_{x_\theta x_\theta}$  can be calculated exactly by Gauss quadrature scheme, so the derivatives are accurate.

The coordinates of points  $p_1$ ,  $p_2$  and  $p_3$ , which have been obtained from Eq. (1), are sufficient to calculate the face integral in Eq. (39) and Eq. (41), so no extra information is needed to calculate these derivatives.

The final algorithm for accurately calculating the analytical derivative are shown below:

1. Solve the local volume enforcement Eq. (1) to determine the approximate surface and save the coordinates of the base surface's vertices  $p_i$ .
2. Calculate the centroid of the base surface and establish the local coordinate system according to Eq. (24) and Eq. (26).
3. Transform the global coordinates of  $p_i$ ,  $\mathbf{x}(\theta, \varphi)$  and  $\mathbf{x}^{\text{ref}}$  into the local coordinate system.
4. Calculate the integrals in Eq. (39) and Eq. (41) to obtain the partial derivatives of  $\mathbf{x}_m$  with respect to  $\theta$  and  $\varphi$ .
5. Calculate the analytical partial derivatives by Eq. (5) and Eq. (6).

## 6. Numerical experiments

In this section, the analytical partial derivatives are firstly validated in Section 6.1 and then the accuracy, efficiency and robustness of the improved MoF method are investigated in Section 6.2.

### 6.1. Single cell test

The analytical derivatives are first validated on a single cell shown in Fig. 6 with vertices  $A(0, 0, 0)$ ,  $B(1.1, 0, 0)$ ,  $C(1, 1.2, 0)$ ,  $D(0, 1.3, 0.2)$ ,  $P(0, 0, 1.2)$ ,  $Q(1, 0, 1.1)$ ,  $R(1, 1.2, 1.1)$  and  $S(0, 1, 1.3)$ . The cell is a generalized hexahedron because its vertices do not lie on the same plane in every face, therefore the face centers are also shown in the hexahedron and each face is decomposed into four triangles as in Jia et al. (2013) [12] and Ahn et al. (2007) [19].

#### 6.1.1. Convergence test at a single sample point

Suppose the volume fraction of the cell is prescribed as  $f = 0.32$ , the reference centroid is  $\mathbf{x}^{\text{ref}} = (0.2, 0.2, 0.2)$  and the sample point is  $\theta = 0.37\pi$ ,  $\varphi = 0.14\pi$ . The numerical partial derivatives are

$$[f, \theta]_{\text{num}} = \frac{f(\theta + \Delta\theta, \varphi) - f(\theta, \varphi)}{\Delta\theta} \quad (42)$$

$$[f, \varphi]_{\text{num}} = \frac{f(\theta, \varphi + \Delta\varphi) - f(\theta, \varphi)}{\Delta\varphi} \quad (43)$$

which are first order accurate. The numerical derivatives depend on the increments  $\Delta\theta$  and  $\Delta\varphi$  and they will be more accurate as the increments decrease. On the contrary, the analytical derivatives are independent of  $\Delta\theta$  and  $\Delta\varphi$  so this test

**Table 1**  
Discrepancy between the numerical and analytical partial derivatives.

$\Delta\theta$ or $\Delta\varphi$	$ [f,\theta]_{\text{num}} - f,\theta $	$ [f,\varphi]_{\text{num}} - f,\varphi $
$1 \times 10^{-2}$	$1.96 \times 10^{-3}$	$1.80 \times 10^{-3}$
$1 \times 10^{-3}$	$1.96 \times 10^{-4}$	$1.81 \times 10^{-4}$
$1 \times 10^{-4}$	$1.96 \times 10^{-5}$	$1.81 \times 10^{-5}$
$1 \times 10^{-5}$	$1.96 \times 10^{-6}$	$1.81 \times 10^{-6}$
$1 \times 10^{-6}$	$1.96 \times 10^{-7}$	$1.81 \times 10^{-7}$

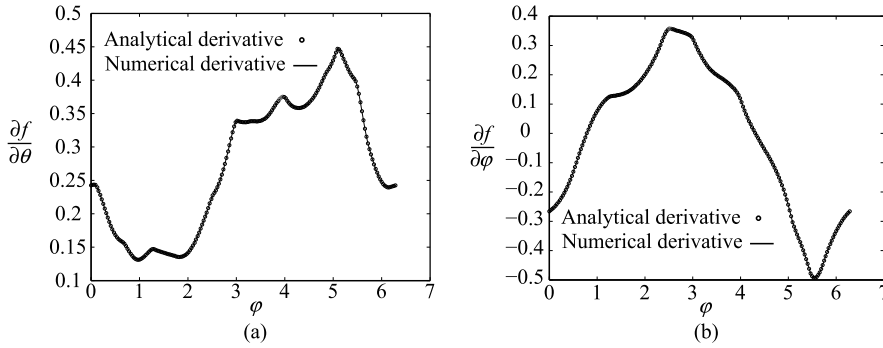


**Fig. 7.** Derivative comparison along a line with  $\theta = 0.37\pi$ .

is to decrease  $\Delta\theta$  and  $\Delta\varphi$  gradually to make the numerical derivatives more accurate and see their differences with the analytical partial derivatives.

Table 1 lists the discrepancy between the numerical partial derivatives and the analytical partial derivatives at the sample point. As expected, the numerical partial derivatives converge to the analytical partial derivatives at first order convergence rate, which means that the analytical partial derivatives given in this paper are the exact derivatives.

6.1.2. Test at sample points on a line

The convergence rate is merely tested at one sample point in Table 1. To test at sample points on a line,  $\theta = 0.37\pi$  is fixed and  $\varphi$  has values from 0 to  $2\pi$  with an increment of  $\delta\varphi = 0.01\pi$ . The analytical derivatives and the numerical derivatives with respect to  $\theta$  and  $\varphi$  are calculated at each sample point and the results are compared in Fig. 7(a) and Fig. 7(b), in which the solid lines denote the numerical derivatives with the increment of  $\theta$  and  $\varphi$  equal to  $10^{-6}$  and the dots denote the analytical derivatives. It can be seen that the numerical derivatives and the analytical derivatives are almost exactly coincident at all sample points.

6.2. Surface reconstructions

In this section, we will study the efficiency and robustness improvement achieved by the analytical derivatives. The efficiency is improved in two ways. Firstly, the analytical derivatives are obtained by solving Eq. (1) only once while the numerical derivatives need to solve Eq. (1) three times when evaluating the partial derivatives at each iterative point  $(\theta, \varphi)$ . As solving Eq. (1) will consume most of CPU time, this part will lead to about 3 times of efficiency improvement. Secondly, the numerical derivatives are only first order accurate, therefore, the number of iterative steps using the analytical derivatives will be less than that using the numerical derivatives. Meanwhile, the quasi-Newton iteration with the analytical derivatives will be more stable and robust than that with the numerical derivatives. It is hard to estimate the efficiency improvement of this part quantitatively because the smoothness and convexity of the objective functions vary significantly in different problems, but in general, the less smooth and convex a objective function is, the more improvement will be achieved using the analytical derivatives.

Planar surface reconstruction is performed in Section 6.2.1, in which the objective function is smooth and convex enough so the efficiency improvement is achieved mainly from the first part. Subsequently, a ‘‘C’’ shaped column reconstruction is performed in Section 6.2.2, which includes planar surfaces, smooth surfaces and discontinuous surfaces so the efficiency and robustness improvement is achieved from both parts. Finally, a more complex example containing three materials is presented in Section 6.2.3 which demonstrates the analytical partial derivatives are applicable on arbitrary convex polyhedron.

The  $\Delta\theta$  and  $\Delta\varphi$  in numerical derivatives equal to  $10^{-8}$  in Section 6.2.1 and  $10^{-7}$  in Section 6.2.2 and Section 6.2.3.

6.2.1. Planar surfaces reconstruction test

A series of target planar surfaces are reconstructed in the single cell shown in Fig. 6 with the same volume fraction  $f = 0.32$ . The normal of these target surfaces are prescribed by  $\theta$  varied from 0 to  $\pi$  and  $\varphi$  varied form 0 to  $2\pi$  with an increment of  $\delta\theta = \delta\varphi = 0.01\pi$ . Based on each determined target surface normal  $\mathbf{n}_i$ , Eq. (1) is solved to obtain the

**Table 2**  
Efficiency improvement in planar surface reconstruction.

Type of derivatives	CUP time	Average number of iterative steps
Numerical	8.61 s	9.30
Analytical	3.07 s	9.30

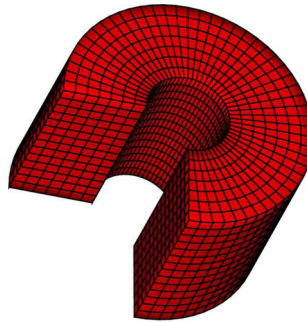


**Fig. 8.** The FEM model of the “C” shaped column whose surface is to be reconstructed.

constant  $d^*$ . Then the polyhedron below the target surface is constructed to calculate the reference centroid  $\mathbf{x}_{m,i}$ . Finally,  $f$  and  $\mathbf{x}_{m,i}$  are used in MoF method to reconstruct this target plane. While the MoF method reconstructs a plane exactly, the resulted normal must equal to  $\mathbf{n}_i$  within a small tolerance. The BFGS quasi-Newton iteration [24] with Wolfe inaccurate one dimension searching [25] is used to solve the optimization and the convergence tolerance is chosen as  $\|\nabla f\| = \sqrt{(\partial f/\partial\theta)^2 + (\partial f/\partial\varphi)^2} < 10^{-8}$  where  $f$  is the objective function in Eq. (2).

The CPU time and average number of iterative steps used by surface reconstruction with the numerical derivatives and the analytical derivatives are compared in Table 2. The average number of iterative steps is the same no matter whether using the numerical derivatives or the analytical derivatives. Thus, the convergence rate does not depend on the choice of derivatives in the planar surfaces reconstruction because its objective function is convex and smooth enough. Therefore, the efficiency improvement in this example is mainly achieved from the first part, namely about 2.80 times improvement which is little less than expected 3 times because there is minor extra effort in calculating the analytical derivatives. The differences between the target normal and the reconstructed normal are about  $10^{-7}$  for both numerical derivatives and analytical derivatives, which will be decreased with the decrease of the convergence tolerance. Therefore, the MoF method can reconstruct a planar surface precisely.

### 6.2.2. “C” shaped column reconstruction

The “C” shaped column shown in Fig. 8 is reconstructed on both regular and distorted grids. This column is an FEM model discretized by hexahedron elements and its surface is going to be reconstructed. The regular grid is  $50 \times 50 \times 50$  orthogonal equidistant on  $(0, 1) \times (0, 1) \times (0, 1)$  and the distorted grid is constructed by moving the nodes of the regular grid as in Garimella et al. (2007) [13], namely

$$x' = x_0 + 0.1 \sin(2\pi x_0) \sin(2\pi y_0) \sin(2\pi z_0)$$

$$y' = y_0 + 0.1 \sin(2\pi x_0) \sin(2\pi y_0) \sin(2\pi z_0)$$

$$z' = z_0 + 0.1 \sin(2\pi x_0) \sin(2\pi y_0) \sin(2\pi z_0)$$

where  $x'$ ,  $y'$  and  $z'$  are the coordinates of the distorted grid nodes and  $x_0$ ,  $y_0$  and  $z_0$  are the coordinates of the corresponding regular ones. The initial volume fraction and material centroid are obtained by intersecting the hexahedron elements in the FEM model with the cells in the computational grid and calculating the integrals on the intersected portion. It should be mentioned that the column is inclined and its edges are not coincident with the computational grid lines so unsmooth surface may appear in some cells near the edge. There are 4569 and 5416 mix cells in the regular and distorted grids, respectively.

The reconstructed “C” shaped columns on the regular and distorted grids are shown in Fig. 9 and Fig. 10, respectively. The smooth surfaces of the column can be reconstructed with high accuracy, whereas the nonsmooth surfaces near the edge can not be reconstructed accurately because the two different surfaces are located in one cell which can not be approximated by only one plane. These different regions are labeled in Fig. 9(a) and they are analogous in other figures.

Although there is no obvious difference observed between the columns reconstructed with the analytical derivatives and the numerical derivatives, the efficiency and robustness improvement can be achieved from both parts because the objective functions in this example are not as smooth and convex as those in the planar surfaces reconstruction.

Table 3 compares the efficiency of the “C” shaped column reconstruction on the regular grid, which shows that about 3.58 times efficiency improvement is achieved by using the analytical derivatives, which is higher than that in planar surface

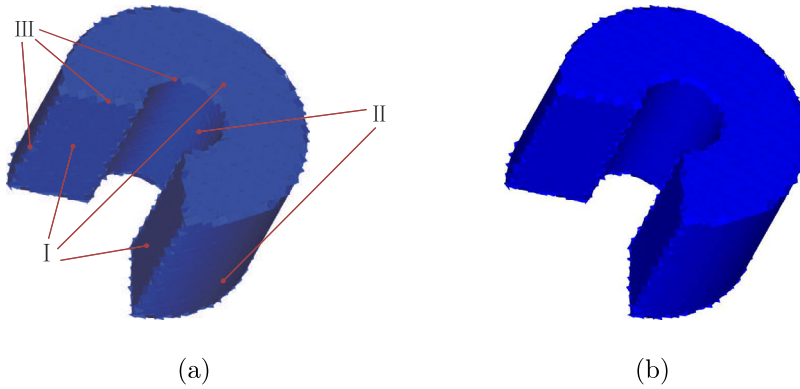


**Fig. 9.** “C” shaped column reconstructed on the regular grid with (a) numerical derivatives and (b) analytical derivatives. The regions I and II in (a) are the smooth surfaces which can be reconstructed with high accuracy, whereas the region III is near the edge of the column which is nonsmooth so they can not be reconstructed accurately. For a clear interpretation of this figure, the electronic version of this paper is recommended.

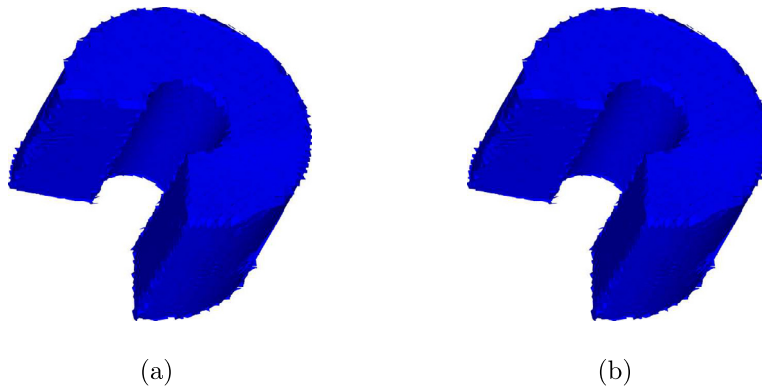


**Fig. 10.** “C” shaped column reconstructed on the distorted grid (a) with numerical derivatives and (b) with analytical derivatives. For a clear interpretation of this figure, the electronic version of this paper is recommended.

**Table 3**  
Efficiency comparison on the regular grid.

Type of derivatives	CPU time	Average number of iterative steps	
		BFGS	1D searching
Numerical	10.59 s	5.52	1.38
Analytical	2.96 s	5.36	1.20

reconstruction. The extra improvement is achieved due to the reduced number of iterative steps. The average number of iterative steps in both BFGS process and 1D searching process are reduced by using the analytical derivatives. Moreover, 2 mix cells are not converged when using the numerical derivatives. The non-convergence may be attributed to several reasons such as the iterative error in solving Eq. (1), the numerical error in clipping and capping algorithm or the numerical error from the differential derivatives, etc. These errors will result in the oscillation of the iterative point near the optimal solution and could not be converged within the given small tolerance ( $10^{-6}$  in this example). However, all mix cells are converged when using analytical derivatives because there is no error in derivatives, but if the tolerance comes to less than  $10^{-8}$ , non-convergence will also occur due to other errors. Nevertheless, the robustness of the iteration is indeed improved significantly by using the analytical derivatives.

In the reconstruction on the distorting grid, more efficiency improvement is achieved from the second part. As shown in Table 4, 3.94 times efficiency improvement is achieved which is higher than that achieved on the regular grid because the distorting grid undermines the smoothness and convexity of the objective functions. Similarly, the average number of iterative steps in BFGS process and 1D searching process are reduced when using the analytical derivatives, especially in 1D searching. In this example, 7 mix cells are not converged when using the numerical derivatives while all mix cells are converged when using the analytical derivatives, so the analytical derivatives improve the robustness significantly when the smoothness and convexity of the objective function are corrupted.

**Table 4**  
Efficiency comparison on the distorted grid.

Type of derivatives	CPU time	Average number of iterative steps	
		BFGS	1D searching
Numerical	21.85 s	9.44	1.69
Analytical	5.54 s	9.40	1.24

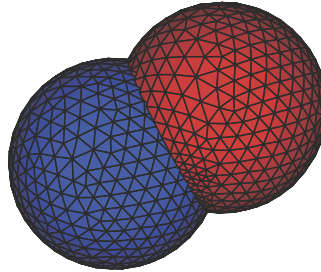


**Fig. 11.** Multi-material FEM model of two intersected spheres. Two intersected spheres  $S_1$  and  $S_2$  with radius  $r = 0.3$  which centered at  $(0.4, 0.4, 0.4)$  and  $(0.6, 0.6, 0.6)$  define three materials: material 1 is defined by  $S_1$  (blue), material 2 is by  $S_2 - S_1$  (red) and material 3 is the background which is not shown in the figure. (For interpretation of the references to color in this figure legend, the reader is referred to the web version of this article.)

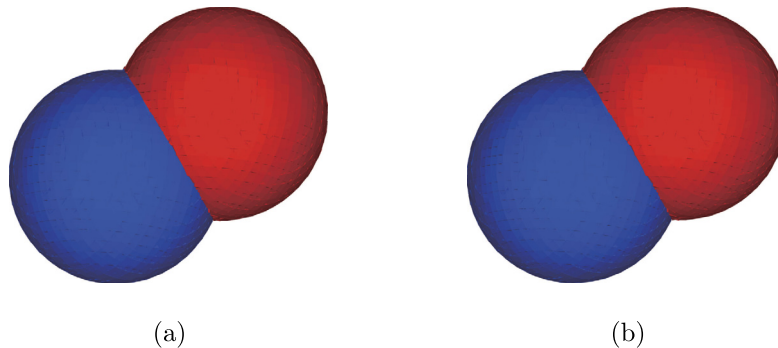


**Fig. 12.** The reconstructed surfaces of two intersected spheres using numerical derivatives (a) and analytical derivatives (b).

### 6.2.3. Multi-material surface reconstruction

The surfaces of two intersected spheres will be reconstructed in this section, whose FEM model is shown in Fig. 11. The two spheres, denoted by  $S_1$  and  $S_2$ , are centered at  $(0.4, 0.4, 0.4)$  and  $(0.6, 0.6, 0.6)$  with radius  $r = 0.3$ . They define three materials: material 1 is defined by  $S_1$  (blue), material 2 is by  $S_2 - S_1$  (red) and material 3 is the background which is not shown in the figure for visualization purposes. The computational grid is  $40 \times 40 \times 40$  orthogonal equidistant on  $(0, 1) \times (0, 1) \times (0, 1)$  which is same as that in Ahn et al. [19]. The initial reference volume fraction and material centroid are obtained by the method described in Section 6.2.2.

In this example, three different materials will simultaneously attend in the cells near the intersection line of the spheres and these cells will be sub-divided into three portions. The optimal reconstruction order can be obtained automatically in MoF method [18,19] and in the second sub-division, the MoF method will be performed on an arbitrary irregular polyhedron.

The reconstructed surface by numerical and analytical partial derivatives are shown in Fig. 12. The surfaces can be effectively reconstructed by both approaches and the results are almost the same as that in Ahn et al. [19]. Although there is no obvious difference in the figures, the efficiency and robustness results listed in Table 5 show the significant advantage of the analytical derivatives. A 3.19 times efficiency improvement is achieved by using the analytical derivatives and all mixed cells converge with the given tolerance. Moreover, all the 19 non-convergent cells using numerical derivatives contain three materials simultaneously which indicates that the analytical derivatives improve the robustness remarkably on arbitrary irregular polyhedrons.

**Table 5**  
The efficiency and robustness result of multi-material reconstruction.

Type of derivatives	CPU time	Non-convergent cases
Numerical	11.11	19
Analytical	3.48	0

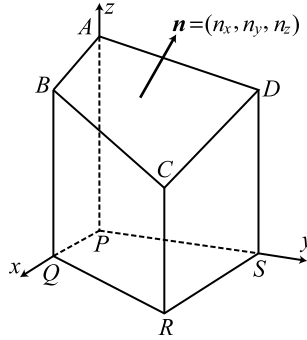


**Fig. 13.** Volume integral in a column.

**7. Conclusion**

In this paper, the analytical first order derivatives of the objective function in MoF surface reconstruction is deduced through a geometric analysis. The value of the objective function and its partial derivatives can be calculated simultaneously without extra objective function calculations which is required in the finite difference approximation. Moreover, a general centroid rotation rule is proposed to fulfill the local volume enforcement which is applicable in any kinds of VoF algorithms. The numerical experiments show that the analytical derivatives are the limits of the finite differential derivatives as  $\Delta\varphi$  and  $\Delta\theta$  approach to zero, which validates the analytical derivatives. Finally, the numerical experiments on planar surface, “C” shaped column and two intersected spheres indicate the iteration with the analytical derivatives is more robust and about 3 to 4 times faster than that using the numerical derivatives. In general, when the smoothness and convexity of the objective functions are corrupted by discontinuous surface or distorting grid, significant robustness and efficiency improvement will be achieved by using the analytical derivatives.

**Acknowledgements**

This work was supported by the National Natural Science Foundation of China (Grant Nos. 11390363 and 11272180).

**Appendix A. Volume integral in a column**

As shown in Fig. 13, the polyhedron  $ABCDPQRS$  is a column, namely edge  $AP, BQ, CR$  and  $DS$  are all vertical to the bottom-surface. In order to calculate its volume  $V = \int_{\Omega} dV$ , the volume integral can be converted into surface integrals by using the Gauss theory as

$$\int_{\Omega} dV = \sum_i \oint_{\Pi_i} \mathbf{n}_i \cdot \mathbf{g} dS \tag{A.1}$$

where  $\mathbf{g} = (0, 0, z)$ . Therefore, Eq. (A.1) can be rewritten as

$$\int_{\Omega} dV = \sum_i \oint_{\Pi_i} n_{iz} z dS \tag{A.2}$$

Because  $n_{iz} = 0$  on all side-faces of the column and  $z = 0$  on the bottom-face of the column, there is only one non-zero term in the right side of Eq. (A.2), thus

$$\int_{\Omega} dV = n_z \oint_{ABCD} z dS \tag{A.3}$$

Therefore, the volume integral on a column can be converted into a surface integral on the top surface of the column, which is much easier to be calculated. Moreover, if the equation of the plane  $ABCD$  is  $z = ax + by + c$ , the surface integral on  $ABCD$  can be converted to a integral on the bottom-surface of the column as

$$\int_{\Omega} dV = n_z \oint_{ABCD} z dS = \text{sign}(n_z) \oint_{PQRS} (ax + by + c) dx dy \quad (\text{A.4})$$

In order to calculate the centroid of the column, only  $\mathbf{g}$  in Eq. (A.1) is different, namely

$$\int_{\Omega} x dV = n_z \oint_{ABCD} x z dS = \text{sign}(n_z) \oint_{PQRS} (ax + by + c) x dx dy \quad (\text{A.5})$$

$$\int_{\Omega} y dV = n_z \oint_{ABCD} y z dS = \text{sign}(n_z) \oint_{PQRS} (ax + by + c) y dx dy \quad (\text{A.6})$$

$$\int_{\Omega} z dV = \frac{1}{2} n_z \oint_{ABCD} z^2 dS = \frac{1}{2} \text{sign}(n_z) \oint_{PQRS} (ax + by + c)^2 dx dy \quad (\text{A.7})$$

Eq. (A.4) to Eq. (A.7) are volume integrations in a column which were used to calculate the integral in the approximate columns in Section 4 and Section 5.

## References

- [1] A. Bockmann, M. Vartdal, A gradient augmented level set method for unstructured grids, *J. Comput. Phys.* 258 (2014) 47–72.
- [2] R.P. Fedkiw, T. Aslam, B. Merriman, S. Osher, A non-oscillatory Eulerian approach to interfaces in multimaterial flows (the ghost fluid method), *J. Comput. Phys.* 152 (1999) 457–492.
- [3] R.P. Fedkiw, T. Aslam, S. Xu, The ghost fluid method for deflagration and detonation discontinuities, *J. Comput. Phys.* 154 (1999) 393–427.
- [4] D.J. Benson, Volume of fluid interface reconstruction methods for multi-material problems, *Appl. Mech. Rev.* 55 (2002) 151–165.
- [5] J.E. Pilliod, E.G. Puckett, Second-order accurate volume-of-fluid algorithm for tracking material interface, *J. Comput. Phys.* 199 (2004) 465–502.
- [6] E.G. Puckett, A volume-of-fluid interface tracking algorithm with applications to computing shock wave refraction, in: *Proceedings of the 4th International Symposium on Computational Fluid Dynamics*, 1991, pp. 933–938.
- [7] X. Yang, A.J. James, Analytic relations for reconstructing piecewise linear interfaces in triangular and tetrahedral grids, *J. Comput. Phys.* 214 (2006) 41–54.
- [8] C.W. Hirt, B.D. Nichols, Volume of fluid method for the dynamics of free boundary, *J. Comput. Phys.* 39 (1981) 201–255.
- [9] M. Tianbao, W. Cheng, N. Jianguo, Multi-material Eulerian formulations and hydrocode for the simulation of explosions, *Comput. Model. Eng. Sci.* 33 (2008) 155–178.
- [10] D.L. Youngs, Time-dependent multi-material flow with large fluid distortion, in: K.W. Morton, M.J. Baines (Eds.), *Numerical Methods for Fluid Dynamics*, Academic Press, 1982, pp. 273–285.
- [11] J. Lopez, J. Hernandez, Analytical and geometrical tools for 3D volume of fluid method in general grids, *J. Comput. Phys.* 227 (2008) 5939–5948.
- [12] Z. Jia, J. Liu, S. Zhang, An effective integration of methods for second-order three-dimensional multi-material ALE method on unstructured hexahedral meshes using of MOF interface reconstruction, *J. Comput. Phys.* 236 (2013) 513–562.
- [13] R. Garimella, M. Kucharik, M. Shashkov, An effective linearity and bound preserving conservative interpolation (remapping) on polyhedral meshes, *Comput. Fluids* 36 (2007) 224–237.
- [14] H.T. Ahn, M. Shashkov, Geometric algorithms for 3D interface reconstruction, in: *Proceedings of the 16th International Meshing Roundtable*, Springer, Berlin, Heidelberg, 2008, pp. 405–422.
- [15] B. Swartz, The second-order sharpening of blurred smooth borders, *Math. Comput.* 186 (1989) 675–714.
- [16] S.J. Mosso, B.K. Swartz, D.B. Kothe, R.C. Ferrell, A parallel volume-tracking algorithm for unstructured meshes, in: P. Schiano, A. Ecer, J. Periaux, N. Satofuka (Eds.), *Parallel Computational Fluid Dynamic Algorithms and Results Using Advanced Computers*, Elsevier Science, 1997, pp. 368–375.
- [17] H.R. Anbarlooei, K. Mazaheri, Moment of fluid interface reconstruction method in multi-material arbitrary Lagrangian Eulerian algorithm, *Comput. Methods Appl. Mech. Eng.* 198 (2009) 3782–3794.
- [18] V. Dyadechko, M. Shashkov, Reconstruction of multi-material interfaces from moment data, *J. Comput. Phys.* 227 (2008) 5361–5384.
- [19] H.T. Ahn, M. Shashkov, Multi-material interface reconstruction on generalized polyhedral meshes, *J. Comput. Phys.* 226 (2007) 2096–2132.
- [20] M. Kucharik, R.V. Garimella, S.P. Schofield, M.J. Shashkov, A comparative study of interface reconstruction methods for multi-material ALE simulation, *J. Comput. Phys.* 229 (2010) 2432–2452.
- [21] V. Dyadechko, M. Shashkov, Moment-of-fluid interface reconstruction, Tech. rep. LA-UR-05-7571, Los Alamos National Laboratory, Los Alamos, October 2005.
- [22] A. Lemoine, S. Glockner, J. Breil, Moment-of-fluid analytic reconstruction on 2D Cartesian grids, [http://notus-cfd.org/sites/default/files/presentationUSALemoine\\_0.pdf](http://notus-cfd.org/sites/default/files/presentationUSALemoine_0.pdf), January 2016.
- [23] M.B. Stephenson, H.N. Christiansen, A polyhedron clipping and capping algorithm and a display system for three dimensional finite element method, *Comput. Graph.* 9 (1975) 1–16.
- [24] R. Fletcher, A new approach to variable metric algorithms, *Comput. J.* 13 (3) (1970) 317–322.
- [25] R. Fletcher, *Practical Methods of Optimization*, John Wiley and Sons, Ltd., 2000.